Article

Ease of Electrochemical Arsenate Dissolution from FeAsO$_4$ Microparticles during Alkaline Oxygen Evolution Reaction

Published as part of the ACS Organic & Inorganic Au virtual special issue "2023 Rising Stars in Organic and Inorganic Chemistry VSI".

Mrinal Kanti Adak, Hirak Kumar Basak, and Biswarup Chakraborty*

Cite This: ACS Org. Inorg. Au 2023, 3, 223–232 | Read Online

ACCESS | Metrics & More | Article Recommendations | SI Supporting Information

ABSTRACT: Transition metal-based ABO$_4$-type materials have now been paid significant attention due to their excellent electrochemical activity. However, a detailed study to understand the active species and its electro-evolution pathway is not traditionally performed. Herein, FeAsO$_4$, a bimetallic ABO$_4$-type oxide, has been prepared solvothermally. In-depth microscopic and spectroscopic studies showed that the as-synthesized cocoon-like FeAsO$_4$ microparticles consist of several small individual nanocrystals with a mixture of monoclinic and triclinic phases. While depositing FeAsO$_4$ on three-dimensional nickel foam (NF), it can show oxygen evolution reaction (OER) in a moderate operating potential. During the electrochemical activation of the FeAsO$_4$/NF anode through cyclic voltammetric (CV) cycles prior to the OER study, an exponential increment in the current density (j) was observed. An ex situ Raman study with the electrode along with field emission scanning electron microscopy imaging showed that the pronounced OER activity with increasing number of CV cycles is associated with a rigorous morphological and chemical change, which is followed by [AsO$_4$]$^{3-}$ leaching from FeAsO$_4$. A chronoamperometric study and subsequent spectro- and microscopic analyses of the isolated sample from the electrode show an amorphous γ-FeO(OH) formation at the constant potential condition. The in situ formation of FeO(OH)$_{ED}$ (ED indicates electrochemically derived) shows better activity compared to pristine FeAsO$_4$ and independently prepared FeO(OH). Tafel, impedance spectroscopic study, and determination of electrochemical surface area have inferred that the in situ formed FeO(OH)$_{ED}$ shows better electro-kinetics and possesses higher surface active sites compared to its parent FeAsO$_4$. In this study, the electrochemical activity of FeAsO$_4$ has been correlated with its structural integrity and unravels its electro-activation pathway by characterizing the active species for OER.

KEYWORDS: FeAsO$_4$, electro-activation, arsenate leaching, amorphous γ-FeO(OH), electro-active-species
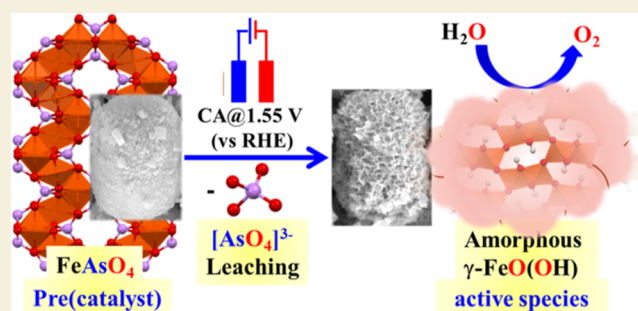
The efficiency of electrochemical water splitting mainly depends on the overpotential and kinetics of oxygen evolution reaction (OER),[1] given that, OER, the anodic reaction, is the potential "bottleneck" of overall water electrolysis.[2,3] However, the OER is necessarily crucial in various energy conversion and storage systems including fuel cells, solar cells, and batteries.[4] For this purpose, the development of a resourceful, stable, and cost-effective electrocatalyst is most important.[5,6] Transition metal-based oxyhydroxides,[7] chalcogenides,[8,9] borides,[10,11] nitrides,[12,13] and phosphides[14,15] have been chosen as better alternatives. Moreover, doping heteroatom, bimetallic, or multimetallic materials with a tunable electronic structure is the current topic of interest.[16] In the heterometallic oxide, typically the first-row transition metal sites are considered to be the true OER sites.[17] The electronic structure and structural rigidity direct the mechanistic pathway of OER.[18]

Transition metal chalcogenides or materials containing non-metals/metalloids are reported to be pre-catalysts, concerning their electrochemical instability and structural transformation during the OER.[3,19] In situ transformation of these pre-catalysts results in formation of metal oxides or metal oxy-hydroxides as active phase and shows higher catalytic activity than the pristine materials.[3,20,21] Better activity arises through surface leaching, reconstruction, or coordination of the adsorbents.[22] Accessible 2e$^-$ redox-couple of "p-block" metal or metalloid oxides makes them fascinating for electrochemical
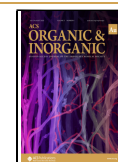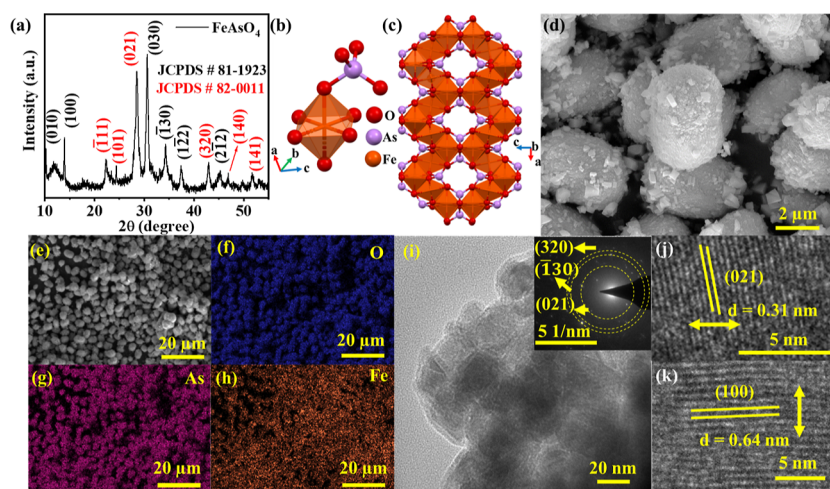
Figure 1. (a) PXRD pattern of the as-synthesized $FeAsO_4$, (b) polyhedral arrangement of the distorted octahedral geometry of $[FeO_6]$ and $[AsO_4]$ unit, (c) three-dimensional spatial orientation of $FeAsO_4$ (in triclinic phase), (d) FESEM image of the as-synthesized $FeAsO_4$, and (e−h) FESEM−EDX elemental mapping of (f) O, (g) As, and (h) Fe. (i) TEM image, (inset) SAED pattern with diffraction rings indexed, (j,k) lattice fringes for (021) and (100) planes of $FeAsO_4$.

studies.[23] In this regard, N-, P-, Sb-, and Bi-containing first-row transition metal oxides show significant impact in the OER study. For example, $Bi_{0.2}Sr_{0.8}CoO_{3−\delta}$,[24] Bi_2WO_6,[25] Ni_2P,[4] $CoBi_2O_2F_4$,[26] $Ni_2P@FePO_xH_y$,[27] $Co_{2−x}Rh_xP$,[28] N-doped CoP,[29] Co_3N,[30] $(Mn_xSb_{1−x})O_2$,[31] and IrO_2-antimony tin oxide[32] show remarkable OER. The mostly explored nitrides and phosphide-based materials are important in the electrocatalytic field owing to their high electroconductivity.[33,34] Though elemental As has semiconductor property, arsenic-based oxides are rarely explored for electrocatalytic OER.[33] However, they are materials for solid-phase energy, superconductivity, and suitable anode Li-ion battery studies.[35−37] In a recent study, Villalobos et al. showed the crucial role of arsenate anions in positioning the cobalt active site within the layered-oxide structure.[38] In another study, NiAs showed higher activity in terms of electrochemically accessible Ni sites and exhibited a higher value of TOF ($0.028\ s^{−1}$) than NiP, NiB, NiTe, and Ni_2Si.[39] Driess et al. prepared FeAs from a 2Fe−2As molecular precursor, which behaved as an electro-(pre)catalyst and under alkaline conditions showed promising OER activity. A detailed study found out that the As leaching resulted in formation of ferrihydrite phase.[33] In this context, the $FeAsO_4$, a class of ABO_4-type material, is least explored as an OER catalyst.

In this work, $FeAsO_4$ prepared solvothermally as micrococoon like particles has been used as anode material to study alkaline OER. Detailed microscopic and spectroscopic studies have been conducted to understand the reactive phase generated during the OER with $FeAsO_4$. According to the ex situ Raman and other microscopic studies, an amorphous γ-FeO(OH) has been formed via rigorous $[AsO_4]^{3−}$ leaching. Operando formation of amorphous FeO(OH) with more exposed surface leads to pronounced OER activity. This study highlights the structure of $FeXO_4$-type material with its electrochemical stability and correlates with their OER activity by providing direct evidence of active species formation.

RESULTS AND DISCUSSION

Via a one-step hydrothermal route, $FeAsO_4$ (Figure S1) material was synthesized in the pure form. In the synthetic procedure, stoichiometric equivalent of ferric chloride, sodium arsenate, was used, and 1:1 ethylene glycol and the water mixture were taken as solvents. After heating the mixture at 160 °C for 12 h, the $FeAsO_4$ material was isolated. In earlier reports, ABO_4-type materials were prepared following a similar procedure.[40−42] However, the morphology and size of the materials varied with the A and B metals present therein. A powder X-ray diffraction (PXRD) study showed numerous reflections, which can be indexed to the reported JCPDS values, and they are also indicative of material's crystallinity. Indexing of the reflections within the 2θ range 20−80° pointed out a mixture of monoclinic (JCPDS #82-0011, space group $P2_1/n$) and triclinic (JCPDS #81-1923, space group $P1$) phase (Figures 1a and S2) with cell parameters for monoclinic phases are a: 7.560, b: 8.081, c: 5.012 and a: 6.600, b: 9.015, c: 6.539 for triclinic phases. The diffraction peaks ($\bar{1}11$), (101), (021), (320), (140), and (141) correspond to the monoclinic phase, whereas (010), (100), (030), ($\bar{1}30$), ($1\bar{2}2$), and ($2\bar{1}2$) are indexed to the triclinic phase. In the repeating unit of the solid state triclinic phase, one $[FeO_6]$ unit is connected to the neighboring $[AsO_4]$ tetrahedron through Fe−μ_2−As−O bridging (Figure 1b), which is distinct from $FeMoO_4$ and $FeWO_4$.[40−42] The distance between a Fe site to its nearest As site is about 2.845−3.415 Å. Three-dimensional arrangement of individual $[FeO_6]$ and $[AsO_4]$ units provides helical-type arrangements (Figure 1c) along the lattice axis a.

The surface morphological and crystallinity of $FeAsO_4$ material were investigated by the field emission scanning electron microscopy (FESEM) and transmission electron microscopy (TEM) analysis (Figure 1d−k). The high-resolution SEM image showed the cocoon-like bulk morphological structures with a mean length of individual cocoon-like particles of ∼2 μm. From the high-resolution image, it is apparent that cocoon-like particles consist of small block shapes particles which were randomly distributed over the surface (Figures 1d and S3 and S4). This typical morphology of the $FeAsO_4$ particles is expected to provide a better surface area during electrocatalytic investigation.[43] The energy-dispersive X-ray (EDX) mapping supported a homogeneous distribution of the constituting elements Fe, As, and O throughout the surface of the particles (Figure 1e−h). Furthermore, the EDX spectra of the studied material

confirmed the existence of Fe and As in an appropriate atomic ratio (Figure S5). The TEM image of the material indicates the presence of nanoscopic particles (Figures 1i and S6), which were agglomerated to form cocoon-like morphology. The selected area electron diffraction (SAED) further pointed out the crystalline nature of the as-synthesized $FeAsO_4$. The diffraction rings in the SAED can be indexed to the crystal planes of (320), ($\overline{1}$30), and (021) owing to their 0.21, 0.25, and 0.31 nm lattice distances, respectively (Figure 1i inset). In the HRTEM images, the lattice fringe lines were identified, where the interplanar distances 0.31 and 0.64 nm correspond to the (021) and (100) planes, respectively, of mixed phase $FeAsO_4$ (Figure 1j,k). The lattice fringes and SAED patterns were in support of the coexistence of the two different phases in synthesized $FeAsO_4$.

$FeAsO_4$ possesses several metal oxygen bonds, and they have active vibrational modes. Raman and Fourier transform infrared (FTIR) spectroscopy analyses were carried out (Figure 2).[2] In the Raman spectra, Raman active bands were
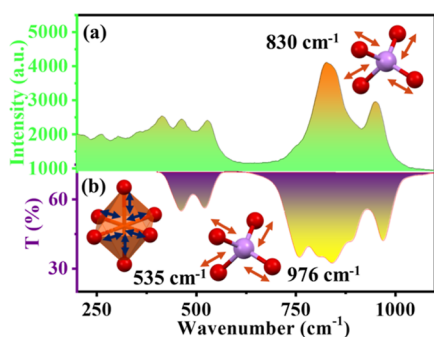

Figure 2. Vibrational spectroscopic study of $FeAsO_4$. Selected region of (a) FTIR and (b) Raman spectra showing two characteristic vibrational modes.

observed at 100 to 1000 cm^{-1} (Figure 2a), which can be well-correlated with the reported scorodite structure.[44] The band position at 350 and 412 cm^{-1} indicates the presence of symmetric bend and antisymmetric bending modes of arsenate, respectively.[45,46] The band at 830 cm^{-1} could be assigned to stretching $[AsO_4]^{3-}$ vibration. The FTIR bands near 3387 and 1634 cm^{-1} indicate the presence of −OH stretching and bending vibration, respectively, owing to the surface-adsorbed moisture (Figure S7). In the spectrum, the As−O stretching vibrations were identified at 976, 841, 768, and 464 cm^{-1}.[44,46−48] The band position near 535 cm^{-1} may be due to Fe−O stretching vibration.[46,49] The Fe−O vibration at a low wavenumber compared to the pure iron oxide sample (584 cm^{-1}) may be due to the presence of the arsenate ion.[49,50] The surface elemental composition was analyzed through the X-ray photoelectron spectroscopy (XPS).[51] The elemental survey scan ensured the presence of desired elements with expected binding energy values for Fe 2p, As 3d, and O 1s (Figure S8a). The high-resolution core-level Fe 2p XP spectrum provided binding energy values at 711.28 and 725.10 eV for Fe $2p_{3/2}$ and Fe $2p_{1/2}$ spin orbit components, respectively (Figure S8b).[4] The deconvoluted Fe 2p XP spectrum provided major contributions at 708.94, 711.28, 712.98, 725.07, and 727.54 eV. A weak contribution of the Fe $2p_{3/2}$ component at 708.94 eV can be attributed to a minor contribution of Fe^{II} present as defect in $FeAsO_4$.[52] However, the bands positioned at 711.28 and 712.98 correspond to Fe^{III}, similar to the reported

value.[4,40] The peak Fe $2p_{1/2}$ spin orbit component of Fe^{III} appeared at 725.07 eV.[49] The core-level XP spectrum of As 3d indicated the presence of As^V owing to the band position at 44.60 eV (Figure S8c).[49] The presence of the oxide ion (O^{2-}) was confirmed from the O 1s major peak position at 530.48 eV, whereas the minor band position at 532.17 eV indicates the existence of some surface adsorbed moisture (Figure S8d).[40,41]

Electrocatalytic OER

The as-synthesized $FeAsO_4$ was studied further as an electrocatalyst for the alkaline (1 M KOH) OER study. A three-electrode cell was used where $FeAsO_4$ deposited (mass loading: 16 mg) on NF, Pt wire, and Hg/HgO were used as working, counter, and reference electrodes (RE), respectively. At first, a cyclic voltammetric (CV) study was performed within the potential range of 1.0−1.9 V [vs reversible hydrogen electrode (RHE)] at a scan rate of 5 mV s^{-1} (Figure 3a). The polarization curves were recorded continuously until a stable current density was achieved at a higher working potential. With the increasing number of CV cycles, the current density at 1.95 V gradually increased and became almost invariable after 6−7 cycles. The highest current density at 1.95 V in the first CV cycle jumped from ∼100 to ca. 275 mA cm^{-2} in the 30th CV cycle. The catalytic current was associated with OER, and huge gas bubbles were formed in the working electrode (WE). Increase in the current density during CV cycles is associated with activation of the catalyst, which can be due to formation of surface-active species. A structural alteration may also be responsible for such huge change in current response in CV cycles. Potential anodic-driven dissolution of the counter anion from the $FeMoO_4$, $NiMoO_4$, covellite CuS, and α-NiS pre-catalyst structures has been identified to be responsible for change in current density.[40,42,53,54] Time-resolved ex situ Raman analysis was thereby performed with the electrode after different CV cycles (1, 5, 10, 20, and 30) to analyze the change of material's associated with the current response observed in the different CV cycles (Figure 3b). With increasing number of CV cycles, time-resolved Raman spectra showed a gradual decrease in the $[AsO_4]^{3-}$ stretching vibration appeared within 800−1000 cm^{-1}. The intensity drops and disappearance of the $[AsO_4]^{3-}$ vibrations after 30 CV cycle implicate a significant amount of arsenate loss from the structure. Moreover, the weak bands appeared at 149, 247, 387, and 520 cm^{-1} in the Raman spectrum after 30 CV cycles was indicative of FeO(OH) phase formation associated with the arsenate loss. A very similar phenomenon has been documented with Fe/$NiMoO_4$.[40,55] To understand further the electrochemical stability of $FeAsO_4$, a freshly deposited $FeAsO_4$ on NF was set at constant operating potential 1.55 V (vs RHE), i.e., CA condition and current response was recorded for over 12 h (Figure 3c). For the initial 2 h, a gradual change in j was noticed. The j went up from 24.6 to 28.3 mA cm^{-2} within first 2.5 h and became constant over the rest 9.5 h. The increment of the j in the CA study is well correlated to the CV cycles (Figure 3a) and due to structural modification of the studied material.[54] A physical change was also observed i.e., the light green color $FeAsO_4$/NF WE turned to red-brown (Figure 3c, inset: top right). The FESEM images acquired with the sample isolated from the electrode after 12 h CA provided a porous morphology, while the shape of the particles remained cocoon-like with rough and porous edges (Figure 3c, inset: top right). The bulk morphology through FESEM provided clear evidence
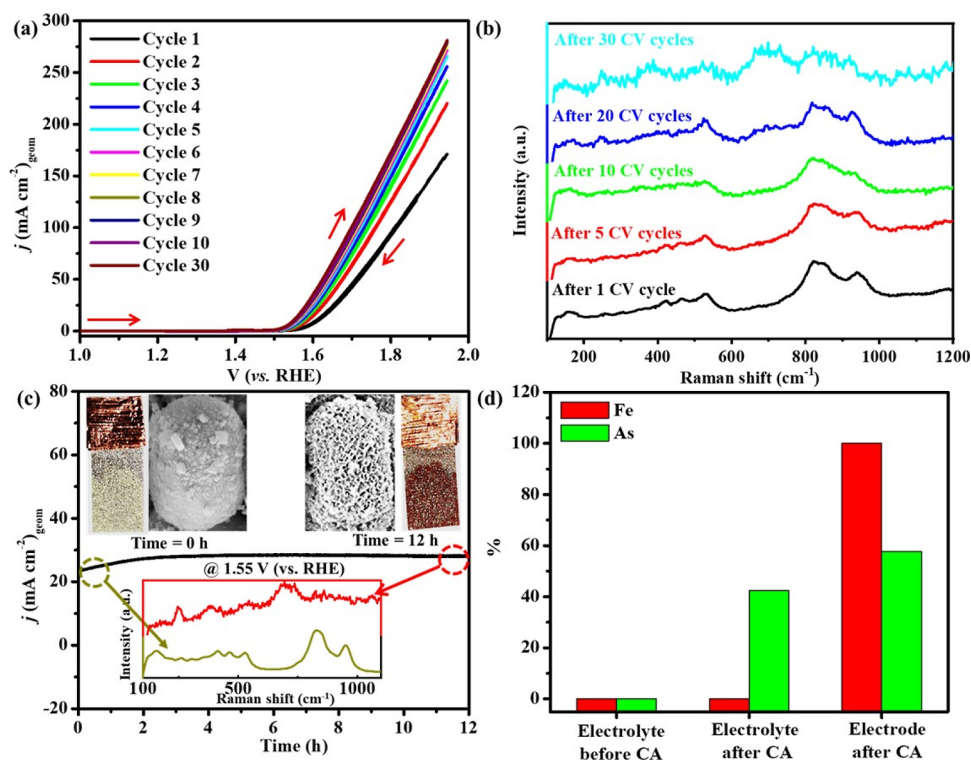
Figure 3. (a) Planograms obtained from the CV cycles recorded with FeAsO$_4$/NF as the working electrode (geometric surface area: 1 cm^2), Pt wire as the counter electrode, and Hg/HgO as the reference electrode, (electrolyte: 1 M KOH, scan rate: 5 mV s^{-1}, cell temp.: room temperature, anodic scan started at 1.0 V), (b) Raman spectra of FeAsO$_4$/NF after different CV cycles mentioned in the inset, (c) chronoamperometric OER (CA) study with FeAsO$_4$/NF at a constant potential of 1.55 V versus RHE (top inset; color changes of the electrode and SEM images and bottom inset: Raman spectra), (d) % of Fe and As found in electrolyte and electrode obtained from the ICP−MS after the 3 h OER-CA study.

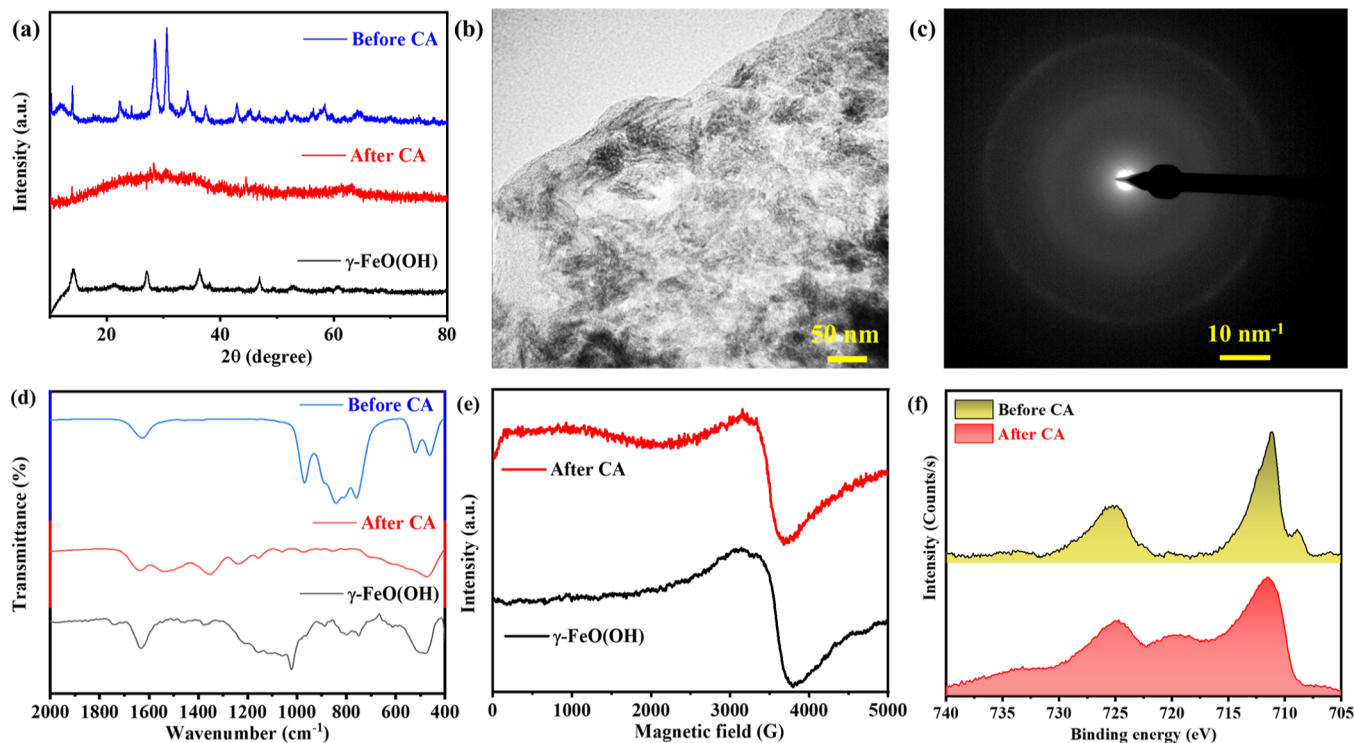**Figure 4.** Post-catalytic characterization of FeAsO$_4$ after 12 h OER-CA analysis; (a) PXRD before and after CA with as-synthesized crystalline γ-FeO(OH), (b) TEM image, (c) SAED pattern, (d) FTIR spectra of FeAsO$_4$ before, after CA and compared with crystalline γ-FeO(OH), (e) EPR spectra of sample isolated after 12 h CA and crystalline γ-FeO(OH), and (f) core-level XP spectra of Fe 2p scan before and after CA.
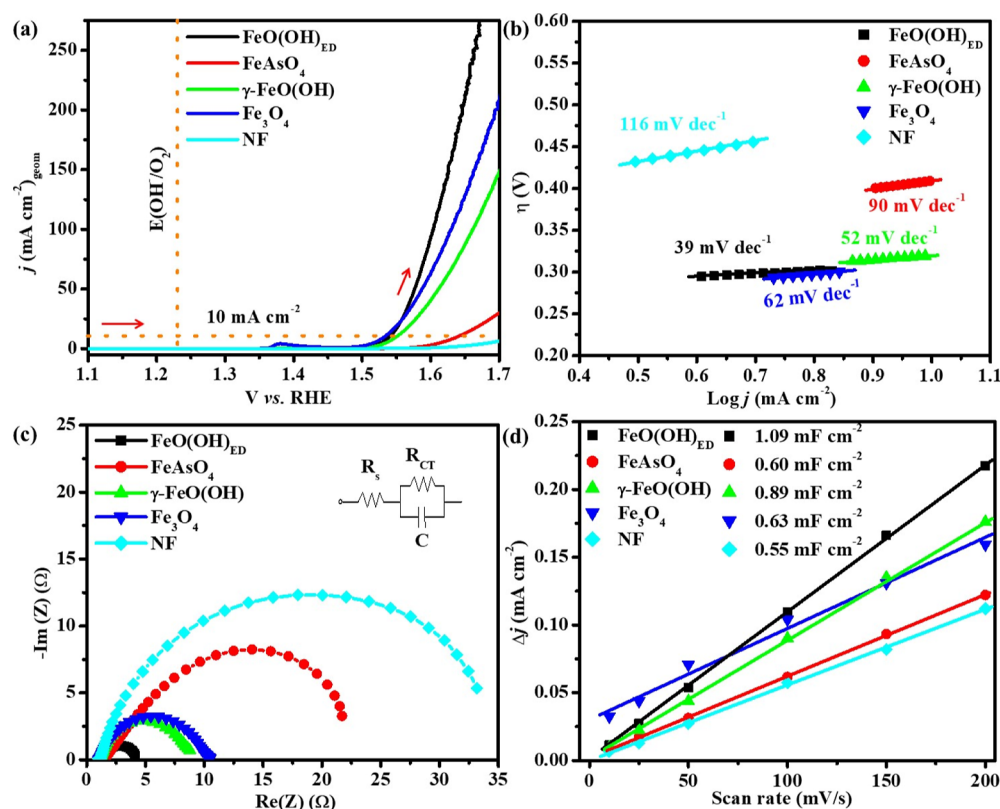
Figure 5. Electrocatalytic OER study. (a) Polarization curves obtained from LSV, (b) Tafel slope, (c) Nyquist plots from EIS data (inset: equivalent circuit fitting), (d) C_{dl} values obtained with FeO(OH)$_{ED}$ (in situ derived from FeAsO$_4$), pristine FeAsO$_4$, independently prepared crystalline γ-FeO(OH), Fe$_3$O$_4$, and NF. (Geometric surface area: 1 cm^2, Pt wire counter electrode, a Hg/HgO RE, electrolyte: 1 M KOH, scan rate: 1 mV s^{-1}, cell temp.: room temperature, scan start: 1.1 V scan end: 1.7 V).

in support of rigorous surface alteration (Figure S9). The EDX elemental mapping and EDX spectrum of the post-catalytic sample provided further evidence in significant $[AsO_4]^{3-}$ loss from the materials after CA (Figures S10 and S11). Some surface-adsorbed $[AsO_4]^{3-}$ may present in the sample, and As in EDX mapping or in the EDX spectrum may presumably be due to the adsorbed arsenate anion. The change of surface morphology indicated the in situ reorganization of and formation of active phases under the CA condition. The Raman spectra of the same material isolated after 12 h CA showed prominent bands at 249, 378, 535, 690−720, and ∼1300 cm^{-1} which are characteristic of the γ-FeO(OH) phase.[7,56] (Figure 3c, inset: down). The pronounced bands of $[AsO_4]^{3-}$ stretching vibrations that vanished after 12 h CA study imply that structural transformation from FeAsO$_4$ to γ-FeO(OH) under alkaline OER conditions is associated with $[AsO_4]^{3-}$ dissolution. It could also be noted that FeAsO$_4$ material is inherently unstable under alkaline conditions, as evident from a control study. A long standing of the FeAsO$_4$/NF electrode in 1 M KOH over a period of 2−4 h resulted in the formation of a significant amount of γ-FeO(OH). Hence, under the electrochemical condition (CV or CA), the rate of structural alternation is accelerated (Figure S12).[40] To identify and quantify the leached species during CA, the electrolyte was analyzed through inductively coupled plasma mass spectrometry (ICP−MS). After 3 h CA, ca. 42.3% As was leached to the electrolyte and no trace of Fe was found in the electrolyte (Figure 3d, Table S1), which indicated the $[AsO_4]^{3-}$ leaching from the FeAsO$_4$.

The samples after 12 h CA were further analyzed by PXRD, and broad diffraction patterns of the suggested amorphous nature of the post-catalytic sample were observed (Figure 4a). In a recent study, the isotypic FeMoO$_4$ also underwent $[MoO_4]^{2-}$ leaching and amorphous α-FeO(OH) formed.[40] In a similar note, NiMoO$_4$ material also undergoes anion dissolution in alkaline conditions to form Ni(OH)$_2$, which then transforms to NiO(OH) under anodic potential.[40,42] However, the amorphous characteristic of electrochemically derived γ-FeO(OH) can further be validated by TEM imaging and SAED pattern obtained with the post-CA sample (Figure 4b,c). The absence of fringe lines in the HRTEM image (Figure S13) further indicated the amorphous phase of FeO(OH). HRTEM also confirms the undefined nanoscopic morphology of the amorphous FeO(OH). The formation of FeO(OH) from the FeAsO$_4$ can also be studied by tracing the As−O stretching vibration, which should be changed after the OER-CA study. The FTIR spectrum of the post-catalytic sample did not show the characteristic $[AsO_4]^{3-}$ vibrations between 750 and 1000 cm^{-1}, which further signifies the potential-driven structural alteration (Figure 4d). From the electron paramagnetic resonance (EPR) of the post-CA sample, the Fe(III) state can be confirmed from the broad axial EPR signal at magnetic fields of 3164 and 3475 gauss. The observed g_1 and g_2 values of 2.16 and 1.91, respectively, correspond to the $s = 1/2$ spin ground state of Fe(III) (Figure 4e).[57] The XPS survey scan showed a significant drop of intensity of As, which is in line with the anion loss proved by other spectroscopic and microscopic study. However, the comparison of core-level Fe 2p scan before and after CA

suggested further pure Fe^{III} state of iron (Figure 4f). Deconvolution of individual Fe $2p_{3/2}$ and $2p_{1/2}$ spin−orbit components (Figure S14) and prominent satellite peak at 719.3 eV were in support of pure Fe^{III}.[40] The core-level O 1s spectrum identified two binding energy values at 530.5 and 531.85 eV, which correspond to O^{2-} and OH^{-}, respectively (Figure S14).[40,58] Thereby, all the spectroscopic and microscopic studies imply a potential-driven transformation of the crystalline $FeAsO_4$ precatalyst to amorphous γ-FeO(OH) active species on the electrode surface.

The abovementioned statements can be validated by comparing the OER activity of $FeAsO_4$ and its electro-derived amorphous γ-FeO(OH). In this regard, polarization curves obtained from the LSV studies (scan rate: 1 mV s^{-1}) with pristine $FeAsO_4$ deposited (16 mg cm^{-2} mass loading) on NF[59] and amorphous γ-FeO(OH) obtained after 30th CV cycles [defined as FeO(OH)$_{ED}$] were compared. The polarization curve for the pristine $FeAsO_4$ delivered an appreciably low j value at 1.7 V (vs RHE), whereas after CV curves recorded under similar electrochemical condition, it showed a high j value at 1.66 V (vs RHE) (Figure 5a and Table S2). The overpotential recorded at a j value of 10 mA cm^{-2} was 310 mV, while the pristine $FeAsO_4$ showed a high overpotential (410 mV) for the same j value. It could be seen that under similar conditions, independently prepared γ-FeO(OH) and Fe_3O_4 (Figure 5a) delivered overpotentials (@10 mA cm^{-2}) of 320 and 303 mV, respectively. The activity of in situ derived FeO(OH)$_{ED}$ was noticeably better than the independently prepared γ-FeO(OH). Although Fe_3O_4 depicted slightly lower overpotential in the kinetic region (low current density region) compared to FeO(OH)$_{ED}$, the catalytic current density above 1.55 V delivered by Fe_3O_4 was significantly lower, which highlighted its poor catalytic OER performance. In comparison, $FeAsO_4$ is least active, while its electro-derived form, i.e., amorphous γ-FeO(OH) showed pronounced activity compared to the independently prepared FeO(OH) (Figure 5a). To correlate its activity with its electro-kinetics, Tafel analysis was performed from the LSV curves recorded at 1 mv s^{-1} scan rate. The Tafel slope of 39 mv dec^{-1} was the lowest among the materials tested herein. It is presumably true that in situ formed FeO(OH) possesses facile electrokinetic during OER, which is neither facilitated by $FeAsO_4$ nor independently prepared using FeO(OH) (Figure 5b and Table S2).[60] Electrochemical impedance spectroscopic (EIS) analysis was further performed to understand the charge-transfer resistance (R_{ct}) exerted by the electrode−electrolyte junction for individual electrodes. At an operating potential of 1.56 V (vs RHE), the Nyquist plot obtained for the FeO(OH)$_{ED}$, $FeAsO_4$, γ-FeO(OH), Fe_3O_4, and NF was a single semicircular arc and can be fitted into a parallel RC circuit. The equivalent circuit fitting provided the R_{ct} value of 2.82, 20.36, 7.44, 9.55, and 31.75 Ω for FeO(OH)$_{ED}$, $FeAsO_4$, γ-FeO(OH), Fe_3O_4, and NF, respectively (Figure 5c). The lowest R_{ct} values for FeO(OH)$_{ED}$ suggest better charge transfer across the electrode−electrolyte interface, which in turn influence dramatically the OER. The large R_{ct} along with the 86 mV dec^{-1} Tafel slope for the pristine $FeAsO_4$ indicated poor charge transfer kinetics in the material itself and the electrode. However, the electrochemically active surface area (ECSA) of the electrode was directly related to the OER activity. ECSA provides an idea about the surface-active species which can be calculated electrochemically from the double-layer capacitance value.[61] C_{dl} recorded from the non-Faradaic CV scans showed

that amorphous γ-FeO(OH)$_{ED}$ has the highest C_{dl} 1.09 mF cm^{-2}. The calculated C_{dl} values were 0.60, 0.89, 0.63, and 0.55 cm^{-2} for $FeAsO_4$, γ-FeO(OH), Fe_3O_4, and NF, respectively which suggested a higher ECSA value of 0.64 (per cm^2 area) for FeO(OH)$_{ED}$ (Figures 5d and S15). The high ECSA value indicates the higher number of surface active sites in amorphous γ-FeO(OH)$_{ED}$, and this is due to rigorous bulk modification. A long-term stability of the electrochemically derived FeO(OH)$_{ED}$ was observed at an applied potential of 1.55 V (vs RHE) for 80 h (Figure S16). The CA study showed that the anode delivered almost constant geometric current density of 25 ($\pm$3) mA cm^{-2} over the time. Almost 12% current fluctuations can be considered as a standard deviation arising from the periodic refilling of the electrolyte. However, 80 h performance with a high catalytic current (i.e., >20 mA cm^{-2}) by the electrode proved its notable long term stability. To showcase further application of the FeO(OH)$_{ED}$ as a potential anode material, a two-electrode electrolyzer was constructed to show overall water splitting (OWS). The performance of the OWS cell, Pt(−)|(+)FeO(OH)$_{ED}$/NF, in 1.0 M KOH was appreciable, as the cell potential of 1.69 V was lower than the cell potential of Pt(−)|(+)NF (1.77 V) and NF(−)|(+)NF (>1.80 V) (Figure S17).

Although the solid-state packing of $FeAsO_4$ lattice and its isotypic ABO_4-type material, $FeMoO_4$, and $NiMoO_4$ reported earlier has a drastic difference, potential-driven AsO_4 leaching is identical to that observed for $FeMoO_4$ and $NiMoO_4$, where the B metal oxyanion undergoes dissolution.[40,42] Anodic potential-driven chemical and structural alternation offers a great opportunity to evolve an active metal oxyhydroxide phase, which can show better activity compared to the same ex situ prepared metal oxyhydroxide. The high-aqueous solubility of the oxyanion $[BO_4]^{n-}$ (B: Mo and As and n: 2 and 3) and also more ionic character of the Fe−O−B result in structural instability under electrochemical conditions.[40] Rapture of the crystalline $FeAsO_4$ microparticles resulted from the hydrolytic dissolution followed by oxidation of the iron sites to the FeO(OH) active phase. In situ transformation on the electrode surface results in random atomic arrangement, and it finally leads to amorphous FeO(OH) active catalysts possessing a high surface area. An in situ derived active catalyst contains more exposed iron sites, which is ideal for a better chemisorption of $[OH]^{-}$ ions on the catalyst's surface and perhaps enhancing the OER on γ-FeO(OH)$_{ED}$.[19,62] In situ grown metal oxy-hydroxide predominantly shows a higher electrochemical surface area compared to ex situ prepared oxyhydroxide, as evident from the experimental data.[63] Furthermore, in situ derived γ-NiOOH from $NiMoO_4$ turned out to be more active than the ex situ prepared NiO(OH).[42] Herein, the dissolution of the $[AsO_4]^{3-}$ leads to vigorous structural alteration and atomic reorientation of the lattice in the iron sites. It may help in the formation of conducting ion channels through the overlapping of transition metal d-shell and oxygen orbitals, which perhaps leads to higher OER activity.[64] In such cases, the place exchange mechanism also plays an important role in the active monolayer formation.[65] The newly formed high energy surface of FeO(OH) with random atomic arrangement leads to facile electro-kinetics and better OER performance, as depicted from the Tafel analysis.[7,56,66,67] Impedance analysis and R_{ct} data indicated further that the formation of amorphous FeO(OH) also helps in a better charge transfer.

CONCLUSIONS

$FeAsO_4$ prepared via a solvothermal route from $FeCl_3$ and Na_2HAsO_4 showed a cocoon-like microstructure, which itself was made of several small individual nanocrystals. However, the as-synthesized $FeAsO_4$ particles consists of a mixture of monoclinic and triclinic phase. The triclinic $FeAsO_4$ phase possessed interconnecting $[FeO_6]$ octahedra and $[AsO_4]$ tetrahedra unlike the previously reported ABO_4-type materials like $FeWO_4$ and $FeMoO_4$, where both the metals adopted octahedral geometry. Via spectroscopic and microscopic characterizations, $FeAsO_4$ was characterized and deposited further on the NF substrate to study OER in alkaline conditions. During CV cycles, the gradual increment in current density followed by the subsequent ex situ Raman study inferred its structural alternation during the electrochemical activation. The CA study followed by detailed microscopic and spectroscopic characterizations indicated its instability and in situ transformation to amorphous γ-$FeO(OH)$ via $[AsO_4]^{3-}$ dissolution. The in situ modification of the $FeAsO_4$ pre-catalyst not only releases the inactive counter anion but also helps to build a highly active $FeO(OH)$ species with a better surface area, which was proved by a detailed electrochemical study and comparing the activity with the pristine $FeAsO_4$ and an independently prepared crystalline γ-$FeO(OH)$. This study showcased a careful spectro-electrochemical analysis on an iron pre-catalyst with a common formula $FeXO_4$ and identification of the electro-evolution pathway to find out the actual active species which was often not emphasized in the traditional OER studies. Further, the $FeAsO_4$ material is a unique example of iron- and arsenic-containing bimetallic oxide which has not yet been explored for the OER study.

EXPERIMENTAL SECTION

Materials and Methods

Materials. $FeCl_3 \cdot 6H_2O$ (Central Drug House (P) Ltd., 98.0%), $Na_2HAsO_4 \cdot 7H_2O$ (Central Drug House (P) Ltd., 99.0%), KOH (Central Drug House (P) Ltd., 85%), and ethylene glycol (Merck India, >99.0%) were used during synthesis and experimental procedures as obtained without additional purification. Nafion (Thermo Fisher, 5% w/w in water and 1-propanol) was used as received. Nickel foam (NF) with 0.2 mm thickness from RVL scientific (India) was used as the electrode support.

Preparation of FeAsO₄. In the synthesis procedure, 1 mmol of $FeCl_3 \cdot 6H_2O$ was taken in a 100 mL round-bottom flask and dissolved in a 10 mL water−ethylene glycol mixture (1:1) with constant stirring on a magnetic stirrer, and then, 1 mmol of $Na_2AsO_4 \cdot 7H_2O$ was added to it. The solution was kept stirring for another 1 h, and the resultant mixture was transferred into a 25 mL Teflon reactor and put inside a stainless-steel autoclave at 160 °C for 12 h. After cooling down to room temperature, the sample was washed with water and ethanol through centrifugation. The material was dried at 60 °C for 2 h in an air oven, and the sample was ground well with agate mortar for further characterization. The synthesized process for $FeAsO_4$ is given stepwise in Figure S1.

Preparation of γ-FeO(OH). Crystalline γ-$FeO(OH)$ was prepared according to the reported procedure and used as reference material.[7]

Electrochemical Study. In the electrocatalytic study, a three-electrode setup was used for the measurement of CV, linear sweep voltammetry (LSV), impedance spectroscopy, and ECSA of the catalyst. The electrocatalytic measurements were conducted in 1 M aqueous KOH solution as an electrolyte. All electrochemical analysis and measurements were performed on a potentiostat (Gamry instruments) instrument controlled by Echem Analyst Software which was also used for further data analysis. In the three-electrode setup, Hg/HgO/NaOH (1 M) (ALS Co. Japan) as a RE, 8 cm Pt spring (ALS Co. Japan) as a counter electrode (CE), and a catalyst loaded NF (0.2 mm thickness, 1 cm^2 geometric surface area, purchased from RVL Scientific, India) as a WE were used during measurement. During the CV and LSV studies, a physical distance of 2 ± 0.2 cm between the working and CE was maintained. All the electrochemical studies were done at room temperature.

Preparation of the WE. The deposition of materials on NF consists of a few steps. At first, NF was cut into 2×1 cm pieces and then washed with hydrochloric acid (0.01 M) through sonication for 10 min, followed by washing with Milli-Q water and acetone and then drying at 50 °C for 8 h. The Nafion solution was diluted with ethanol to 1.0 wt %, and 50 mg $FeAsO_4$ was added to the 1 mL solution.[68] The resulted mixture was ultrasonicated for 10 min. The prepared catalyst ink was then drop-casted through a micro-pipette on (1×1 cm^2) NF surface. The mass loading of the $FeAsO_4$ was optimized to 16 mg per cm^2 geometric surface area of NF. A similar method was also used for the preparation of the γ-$FeO(OH)$ (7 mg) electrode.

Polarization curves from the CV and LSV studies were presented after 85% iR compensation. The potential of the RE is reported versus the RHE and calculated according to the following equation

$$E(RHE) = E(Hg/HgO) + 0.098\,V + (0.059 \times pH)V$$

The potential scan was done between 1.0 and 1.9 V versus RHE and a scan rate of 1 mV s^{-1}. Before the LSV study, CV for 10 cycles was done to activate the catalyst for OER with a 1 mV s^{-1} scan rate. The overpotential was calculated from the resulting polarization curves at 10 mA cm^{-2}. where η = overpotential (V), j = current density (mA cm^{-2}), and b = Tafel slope (mV dec^{-1}). Tafel analysis was done from the data obtain from LSV plot. In the Tafel plot, the overpotentials (η) versus the logarithm of current density was plotted. The following Tafel equation was used to determine the Tafel slope: $\eta = b \log j + a$.

TOF of the catalysts was determined by the use of following equation

$$TOF = \frac{j_{300}\,mV}{\#Fe \times F \times 4}$$

where j = current density at η = 300 mV, $\#Fe$ = the amount of Fe atoms per cm^2 of geometrical electrode area, and F = Faraday constant.

The CA of the deposited catalyst was done in 1 M KOH for examining the long-term stability (12 h). During the stability measurement, a constant current above 10 mA cm^{-2} was applied.

The ECSA of the deposited catalyst was calculated from the double layer capacitance (C_{dl}) value. The C_{dl} values were determined from the CV scans in the non-Faradaic region at different scan rates from 10 to 200 mV s^{-1}. The value of ECSA was calculated from the following equation $ECSA = \frac{C_{dl}}{C_s}$, The value of C_s suggests the specific capacitance of the catalyst per unit area under identical electrolytic conditions.[69] In 1 M KOH electrolyte, the C_s value for NF is 1.06 mF cm^{-2}.[70] EIS of $FeAsO_4/NF$ was studied at 1.56 V vs RHE for Nyquist plots. During the impedance spectroscopy analysis, the selected frequency range was 100 mHz−1 MHz. An equivalent RC circuit model was used to fit the impedance spectra. The charge-transfer resistance (R_{ct}) for the respective catalyst was measured from the Nyquist plot's semicircular diameter.[71]

ASSOCIATED CONTENT

Data Availability Statement

The data for this study are available in the published article and its Supporting Information.

Supporting Information

The Supporting Information is available free of charge at https://pubs.acs.org/doi/10.1021/acsorginorgau.3c00007.

Characterization detail and analysis methods; spectroscopic and microscopic data for $FeAsO_4$ microparticle;

post-catalytic characterization data; and electrochemical data for FeAsO$_4$ and other control materials (PDF)

■ AUTHOR INFORMATION

Corresponding Author

Biswarup Chakraborty − *Department of Chemistry, Indian Institute of Technology Delhi, New Delhi 110016, India;* ● orcid.org/0000-0002-6292-6357; Email: cbiswarup@chemistry.iitd.ac.in

Authors

Mrinal Kanti Adak − *Department of Chemistry, Indian Institute of Technology Delhi, New Delhi 110016, India*

Hirak Kumar Basak − *Department of Chemistry, Indian Institute of Technology Delhi, New Delhi 110016, India*

Complete contact information is available at:
https://pubs.acs.org/10.1021/acsorginorgau.3c00007

Author Contributions

CRediT:**Mrinal Kanti Adak** investigation (lead); methodology (supporting), formal analysis (supporting), writing original draft (supporting), writing-review and editing (supporting); **Hirak Kumar Basak**, investigation (supporting), methodology (supporting), and formal analysis (supporting); **Biswarup Chakraborty** conceptualization (lead), data curation (lead), formal analysis (lead), funding acquisition (lead), methodology (lead), project administration (lead), supervision (lead), validation (lead), writing-original draft (lead), and writing-review and editing (lead).

Notes

The authors declare no competing financial interest.

■ REFERENCES

(1) Evans, T. A.; Choi, K.-S. Electrochemical Synthesis and Investigation of Stoichiometric, Phase-Pure CoSb2O6 and MnSb$_2$O$_6$ Electrodes for the Oxygen Evolution Reaction in Acidic Media. *ACS Appl. Energy Mater.* **2020**, *3*, 5563−5571.

(2) Kou, Z.; Li, X.; Zhang, L.; Zang, W.; Gao, X.; Wang, J. Dynamic Surface Chemistry of Catalysts in Oxygen Evolution Reaction. *Small Sci.* **2021**, *1*, 2100011.

(3) Li, W.; Xiong, D.; Gao, X.; Liu, L. The Oxygen Evolution Reaction Enabled by Transition Metal Phosphide and Chalcogenide Pre-Catalysts with Dynamic Changes. *Chem. Commun.* **2019**, *55*, 8744−8763.

(4) Li, M.; Chen, L.; Ye, S.; Fan, G.; Yang, L.; Zhang, X.; Li, F. Dispersive Non-Noble Metal Phosphide Embedded in Alumina Arrays Derived from Layered Double Hydroxide Precursor toward Efficient Oxygen Evolution Reaction and Biomass Upgrading. *J. Mater. Chem. A* **2019**, *7*, 13695−13704.

(5) Lee, Y.; Suntivich, J.; May, K. J.; Perry, E. E.; Shao-Horn, Y. Synthesis and Activities of Rutile IrO$_2$ and RuO$_2$ Nanoparticles for Oxygen Evolution in Acid and Alkaline Solutions. *J. Phys. Chem. Lett.* **2012**, *3*, 399−404.

(6) Abbott, D. F.; Lebedev, D.; Waltar, K.; Povia, M.; Nachtegaal, M.; Fabbri, E.; Copéret, C.; Schmidt, T. J. Iridium Oxide for the Oxygen Evolution Reaction: Correlation between Particle Size, Morphology, and the Surface Hydroxo Layer from Operando XAS. *Chem. Mater.* **2016**, *28*, 6591−6604.

(7) Mallick, L.; Rajput, A.; Adak, M. K.; Kundu, A.; Choudhary, P.; Chakraborty, B. γ-FeO(OH) with multiple surface terminations: Intrinsically active for the electrocatalytic oxygen evolution reaction. *Dalton Trans.* **2022**, *51*, 15094−15110.

(8) Zhao, X.; Li, X.; Yan, Y.; Xing, Y.; Lu, S.; Zhao, L.; Zhou, S.; Peng, Z.; Zeng, J. Electrical and Structural Engineering of Cobalt Selenide Nanosheets by Mn Modulation for Efficient Oxygen Evolution. *Appl. Catal., B* **2018**, *236*, 569−575.

(9) Hong, Y.-R.; Mhin, S.; Kim, K.-M.; Han, W.-S.; Choi, H.; Ali, G.; Chung, K. Y.; Lee, H. J.; Moon, S.-I.; Dutta, S.; Sun, S.; Jung, Y.-G.; Song, T.; Han, H. Electrochemically Activated Cobalt Nickel Sulfide for an Efficient Oxygen Evolution Reaction: Partial Amorphization and Phase Control. *J. Mater. Chem. A* **2019**, *7*, 3592−3602.

(10) Liu, Q.; Zhao, H.; Jiang, M.; Kang, Q.; Zhou, W.; Wang, P.; Zhou, F. Boron Enhances Oxygen Evolution Reaction Activity over Ni Foam-Supported Iron Boride Nanowires. *J. Mater. Chem. A* **2020**, *8*, 13638−13645.

(11) Cui, L.; Zhang, W.; Zheng, R.; Liu, J. Electrocatalysts Based on Transition Metal Borides and Borates for the Oxygen Evolution Reaction. *Chem.—Eur. J.* **2020**, *26*, 11661−11672.

(12) Wang, C.; Chen, W.; Yuan, D.; Qian, S.; Cai, D.; Jiang, J.; Zhang, S. Tailoring the Nanostructure and Electronic Configuration of Metal Phosphides for Efficient Electrocatalytic Oxygen Evolution Reactions. *Nano Energy* **2020**, *69*, 104453.

(13) Liu, D.; Ai, H.; Li, J.; Fang, M.; Chen, M.; Liu, D.; Du, X.; Zhou, P.; Li, F.; Lo, K. H.; Tang, Y.; Chen, S.; Wang, L.; Xing, G.; Pan, H. Oxygen Evolution Reaction: Surface Reconstruction and Phase Transition on Vanadium−Cobalt−Iron Trimetal Nitrides to Form Active Oxyhydroxide for Enhanced Electrocatalytic Water Oxidation (Adv. Energy Mater. 45/2020). *Adv. Energy Mater.* **2020**, *10*, 2070184.

(14) Cao, L.-M.; Hu, Y.-W.; Tang, S.-F.; Iljin, A.; Wang, J.-W.; Zhang, Z.-M.; Lu, T.-B. Fe-CoP Electrocatalyst Derived from a Bimetallic Prussian Blue Analogue for Large-Current-Density Oxygen Evolution and Overall Water Splitting. *Adv. Sci.* **2018**, *5*, 1800949.

(15) Chen, M.; Li, H.; Wu, C.; Liang, Y.; Qi, J.; Li, J.; Shangguan, E.; Zhang, W.; Cao, R. Interfacial Engineering of Heterostructured Co(OH)$_2$/NiP$_x$ Nanosheets for Enhanced Oxygen Evolution Reaction. *Adv. Funct. Mater.* **2022**, *32*, 2206407.

(16) Zhang, J.; Quast, T.; He, W.; Dieckhöfer, S.; Junqueira, J. R. C.; Öhl, D.; Wilde, P.; Jambrec, D.; Chen, Y.-T.; Schuhmann, W. In Situ Carbon Corrosion and Cu Leaching as a Strategy for Boosting Oxygen Evolution Reaction in Multimetal Electrocatalysts. *Adv. Mater.* **2022**, *34*, 2109108.

(17) Xu, Q.; Jiang, H.; Duan, X.; Jiang, Z.; Hu, Y.; Boettcher, S. W.; Zhang, W.; Guo, S.; Li, C. Fluorination-Enabled Reconstruction of NiFe Electrocatalysts for Efficient Water Oxidation. *Nano Lett.* **2021**, *21*, 492−499.

(18) Han, B.; Grimaud, A.; Giordano, L.; Hong, W. T.; Diaz-Morales, O.; Yueh-Lin, L.; Hwang, J.; Charles, N.; Stoerzinger, K. A.; Yang, W.; Koper, M. T. M.; Shao-Horn, Y. Iron-Based Perovskites for Catalyzing Oxygen Evolution Reaction. *J. Phys. Chem. C* **2018**, *122*, 8445−8454.

(19) Masa, J.; Schuhmann, W. The Role of Non-Metallic and Metalloid Elements on the Electrocatalytic Activity of Cobalt and Nickel Catalysts for the Oxygen Evolution Reaction. *ChemCatChem* **2019**, *11*, 5842−5854.

(20) Wang, X.; Li, W.; Xiong, D.; Petrovykh, D. Y.; Liu, L. Bifunctional Nickel Phosphide Nanocatalysts Supported on Carbon Fiber Paper for Highly Efficient and Stable Overall Water Splitting. *Adv. Funct. Mater.* **2016**, *26*, 4067−4077.

(21) Wang, X.; Li, W.; Xiong, D.; Liu, L. Fast Fabrication of Self-Supported Porous Nickel Phosphide Foam for Efficient, Durable Oxygen Evolution and Overall Water Splitting. *J. Mater. Chem. A* **2016**, *4*, 5639−5646.

(22) Zhao, J.-W.; Shi, Z.-X.; Li, C.-F.; Ren, Q.; Li, G.-R. Regulation of Perovskite Surface Stability on the Electrocatalysis of Oxygen Evolution Reaction. *ACS Mater. Lett.* 2021, 3, 721−737.

(23) Thorarinsdottir, A. E.; Costentin, C.; Veroneau, S. S.; Nocera, D. G. P-Block Metal Oxide Noninnocence in the Oxygen Evolution Reaction in Acid: The Case of Bismuth Oxide. *Chem. Mater.* 2022, 34, 826−835.

(24) Kuznetsov, D. A.; Peng, J.; Giordano, L.; Román-Leshkov, Y.; Shao-Horn, Y. Bismuth Substituted Strontium Cobalt Perovskites for Catalyzing Oxygen Evolution. *J. Phys. Chem. C* 2020, 124, 6562−6570.

(25) Nie, Z.-P.; Ma, D.-K.; Fang, G.-Y.; Chen, W.; Huang, S.-M. Concave Bi_2WO_6 Nanoplates with Oxygen Vacancies Achieving Enhanced Electrocatalytic Oxygen Evolution in Near-Neutral Water. *J. Mater. Chem. A* 2016, 4, 2438−2444.

(26) Yu, X.; Mitoudi-Vagourdi, E.; Johnsson, M. The Aurivillius Compound $CoBi_2O_2F_4$ − an Efficient Catalyst for Electrolytic Water Oxidation after Liquid Exfoliation. *ChemCatChem* 2019, 11, 6105−6110.

(27) Meena, A.; Thangavel, P.; Jeong, D. S.; Singh, A. N.; Jana, A.; Im, H.; Nguyen, D. A.; Kim, K. S. Crystalline-Amorphous Interface of Mesoporous Ni_2P @ $FePO_xH_y$ for Oxygen Evolution at High Current Density in Alkaline-Anion-Exchange-Membrane Water-Electrolyzer. *Appl. Catal., B* 2022, 306, 121127.

(28) Mutinda, S. I.; Li, D.; Kay, J.; Brock, S. L. Synthesis and Characterization of $Co_{2−x}Rh_xP$ Nanoparticles and Their Catalytic Activity towards the Oxygen Evolution Reaction. *J. Mater. Chem. A* 2018, 6, 12142−12152.

(29) Liu, Z.; Yu, X.; Xue, H.; Feng, L. A nitrogen-doped CoP nanoarray over 3D porous Co foam as an efficient bifunctional electrocatalyst for overall water splitting. *J. Mater. Chem. A* 2019, 7, 13242−13248.

(30) Kang, B. K.; Im, S. Y.; Lee, J.; Kwag, S. H.; Kwon, S. B.; Tiruneh, S.; Kim, M.-J.; Kim, J. H.; Yang, W. S.; Lim, B.; Yoon, D. H. In-Situ Formation of MOF Derived Mesoporous Co_3N/Amorphous N-Doped Carbon Nanocubes as an Efficient Electrocatalytic Oxygen Evolution Reaction. *Nano Res.* 2019, 12, 1605−1611.

(31) Zhou, L.; Shinde, A.; Montoya, J. H.; Singh, A.; Gul, S.; Yano, J.; Ye, Y.; Crumlin, E. J.; Richter, M. H.; Cooper, J. K.; Stein, H. S.; Haber, J. A.; Persson, K. A.; Gregoire, J. M. Rutile Alloys in the Mn−Sb−O System Stabilize Mn^{3+} To Enable Oxygen Evolution in Strong Acid. *ACS Catal.* 2018, 8, 10938−10948.

(32) Hartig-Weiss, A.; Miller, M.; Beyer, H.; Schmitt, A.; Siebel, A.; Freiberg, A. T. S.; Gasteiger, H. A.; El-Sayed, H. A. Iridium Oxide Catalyst Supported on Antimony-Doped Tin Oxide for High Oxygen Evolution Reaction Activity in Acidic Media. *ACS Appl. Nano Mater.* 2020, 3, 2185−2196.

(33) Beltrán-Suito, R.; Forstner, V.; Hausmann, J. N.; Mebs, S.; Schmidt, J.; Zaharieva, I.; Laun, K.; Zebger, I.; Dau, H.; Menezes, P. W.; Driess, M. A Soft Molecular 2Fe−2As Precursor Approach to the Synthesis of Nanostructured FeAs for Efficient Electrocatalytic Water Oxidation. *Chem. Sci.* 2020, 11, 11834−11842.

(34) Suen, N.-T.; Hung, S.-F.; Quan, Q.; Zhang, N.; Xu, Y.-J.; Chen, H. M. Electrocatalysis for the Oxygen Evolution Reaction: Recent Development and Future Perspectives. *Chem. Soc. Rev.* 2017, 46, 337−365.

(35) Kamihara, Y.; Watanabe, T.; Hirano, M.; Hosono, H. Iron-Based Layered Superconductor $La[O_{1−x}F_x]$FeAs (x = 0.05−0.12) with Tc = 26 K. *J. Am. Chem. Soc.* 2008, 130, 3296−3297.

(36) Wang, X. C.; Liu, Q. Q.; Lv, Y. X.; Gao, W. B.; Yang, L. X.; Yu, R. C.; Li, F. Y.; Jin, C. Q. The Superconductivity at 18 K in LiFeAs System. *Solid State Commun.* 2008, 148, 538−540.

(37) Parker, D. R.; Pitcher, M. J.; Baker, P. J.; Franke, I.; Lancaster, T.; Blundell, S. J.; Clarke, S. J. Structure, Antiferromagnetism and Superconductivity of the Layered Iron Arsenide NaFeAs. *Chem. Commun.* 2009, 2189−2191.

(38) Villalobos, J.; González-Flores, D.; Klingan, K.; Chernev, P.; Kubella, P.; Urcuyo, R.; Pasquini, C.; Mohammadi, M. R.; Smith, R. D. L.; Montero, M. L.; Dau, H. Structural and Functional Role of Anions in Electrochemical Water Oxidation Probed by Arsenate Incorporation into Cobalt-Oxide Materials. *Phys. Chem. Chem. Phys.* 2019, 21, 12485−12493.

(39) Masa, J.; Piontek, S.; Wilde, P.; Antoni, H.; Eckhard, T.; Chen, Y.-T.; Muhler, M.; Apfel, U.-P.; Schuhmann, W. Ni-Metalloid (B, Si, P, As, and Te) Alloys as Water Oxidation Electrocatalysts. *Adv. Energy Mater.* 2019, 9, 1900796.

(40) Adak, M. K.; Rajput, A.; Ghosh, D.; Chakraborty, B. Role of Fe−O−M Bond in Controlling the Electroactive Species Generation from the $FeMO_4$ (M: Mo and W) Electro(Pre)Catalyst during OER. *ACS Appl. Energy Mater.* 2022, 5, 13645−13660.

(41) Adak, M. K.; Rajput, A.; Mallick, L.; Chakraborty, B. Electrochemically Robust Ferberite ($FeWO_4$) Nanostructure as an Anode Material for Alkaline Water- and Alcohol-Oxidation Reaction. *ACS Appl. Energy Mater.* 2022, 5, 5652−5665.

(42) Rajput, A.; Adak, M. K.; Chakraborty, B. Intrinsic Lability of $NiMoO_4$ to Excel the Oxygen Evolution Reaction. *Inorg. Chem.* 2022, 61, 11189−11206.

(43) Mandal, M.; Subudhi, S.; Nayak, A. K.; Alam, I.; Subramanyam, B. V. R. S.; Maheswari, R. P.; Patra, S.; Mahanandia, P. In-Situ Synthesis of Mixed-Phase Carbon Material Using Simple Pyrolysis Method for High-Performance Supercapacitor. *Diamond Relat. Mater.* 2022, 127, 109209.

(44) Ma, X.; Zhang, J.; Gomez, M. A.; Ding, Y.; Yao, S.; Lv, H.; Wang, X.; Wang, S.; Jia, Y. Partitioning and Transformation Behavior of Arsenic during Fe(III)-As(III)-As(V)-$SO_4^{2−}$ Coprecipitation and Subsequent Aging Process in Acidic Solutions: Implication for Arsenic Mobility and Fixation. *Sci. Total Environ.* 2021, 799, 149474.

(45) Frost, R. L.; Weier, M. L.; Williams, P. A.; Leverett, P.; Kloprogge, J. T. Raman Spectroscopy of the Sampleite Group of Minerals. *J. Raman Spectrosc.* 2007, 38, 574−583.

(46) Gomez, M. A.; Assaaoudi, H.; Becze, L.; Cutler, J. N.; Demopoulos, G. P. Vibrational Spectroscopy Study of Hydrothermally Produced Scorodite ($FeAsO_4 \cdot 2H_2O$), Ferric Arsenate Sub-Hydrate (FAsH; $FeAsO_4 \cdot 0.75H_2O$) and Basic Ferric Arsenate Sulfate (BFAS; $Fe[(AsO_4)_{1−x}(SO_4)_x(OH)_x] \cdot wH_2O$). *J. Raman Spectrosc.* 2010, 41, 212−221.

(47) Gomez, M. A.; Becze, L.; Celikin, M.; Demopoulos, G. P. The Effect of Copper on the Precipitation of Scorodite ($FeAsO_4 \cdot 2H_2O$) under Hydrothermal Conditions: Evidence for a Hydrated Copper Containing Ferric Arsenate Sulfate-Short Lived Intermediate. *J. Colloid Interface Sci.* 2011, 360, 508−518.

(48) Ondruš, P.; Skála, R.; Viti, C.; Veselovský, F.; Novák, F.; Jansa, J. Parascorodite, $FeAsO_4.2H_2O$; a new mineral from Kank near Kutna Hora, Czech Republic. *Am. Mineral.* 1999, 84, 1439−1444.

(49) Dutta, S.; Manna, K.; Srivastava, S. K.; Gupta, A. K.; Yadav, M. K. Hollow Polyaniline Microsphere/Fe_3O_4 Nanocomposite as an Effective Adsorbent for Removal of Arsenic from Water. *Sci. Rep.* 2020, 10, 4982.

(50) Shabnam, R.; Rahman, M. A.; Miah, M. A. J.; Sharafat, M. K.; Islam, H. M. T.; Gafur, M. A.; Ahmad, H. Novel Magnetically Doped Epoxide Functional Cross-Linked Hydrophobic Poly(Lauryl Methacrylate) Composite Polymer Particles for Removal of As(III) from Aqueous Solution. *Ind. Eng. Chem. Res.* 2017, 56, 7747−7756.

(51) Mitchell, C. E.; Santos-Carballal, D.; Beale, A. M.; Jones, W.; Morgan, D. J.; Sankar, M.; de Leeuw, N. H. The Role of Surface Oxidation and Fe−Ni Synergy in Fe−Ni−S Catalysts for CO_2 Hydrogenation. *Faraday Discuss.* 2021, 230, 30−51.

(52) Rajan, A.; Sharma, M.; Sahu, N. K. Assessing Magnetic and Inductive Thermal Properties of Various Surfactants Functionalised Fe_3O_4 Nanoparticles for Hyperthermia. *Sci. Rep.* 2020, 10, 15045.

(53) Dürr, R. N.; Maltoni, P.; Tian, H.; Jousselme, B.; Hammarström, L.; Edvinsson, T. From $NiMoO_4$ to γ-NiOOH: Detecting the Active Catalyst Phase by Time Resolved in Situ and Operando Raman Spectroscopy. *ACS Nano* 2021, 15, 13504−13515.

(54) Kundu, A.; Adak, M. K.; Kumar, Y.; Chakraborty, B. Electrochemically Derived Crystalline CuO from Covellite CuS Nanoplates: A Multifunctional Anode Material. *Inorg. Chem.* 2022, 61, 4995−5009.

(55) Liu, L.; Corma, A. Structural Transformations of Solid Electrocatalysts and Photocatalysts. *Nat. Rev. Chem.* **2021**, *5*, 256−276.

(56) Adak, M. K.; Mallick, L.; Samanta, K.; Chakraborty, B. Slow O−H Dissociation in the First-Order Oxygen Evolution Reaction Kinetics on Polycrystalline γ-FeO(OH). *J. Phys. Chem. C* **2023**, *127*, 154.

(57) Sayler, R. I.; Hunter, B. M.; Fu, W.; Gray, H. B.; Britt, R. D. EPR Spectroscopy of Iron- and Nickel-Doped [ZnAl]-Layered Double Hydroxides: Modeling Active Sites in Heterogeneous Water Oxidation Catalysts. *J. Am. Chem. Soc.* **2020**, *142*, 1838−1845.

(58) Kong, L.; Zhang, M.; Liu, X.; Ma, F.; Wei, B.; Wumaier, K.; Zhao, J.; Lu, Z.; Sun, J.; Chen, J.; Gao, F. Green and Rapid Synthesis of Iron Molybdate Catalyst by Mechanochemistry and Their Catalytic Performance for the Oxidation of Methanol to Formaldehyde. *Chem. Eng. J.* **2019**, *364*, 390−400.

(59) Liu, B.; Zhao, Y.-F.; Peng, H.-Q.; Zhang, Z.-Y.; Sit, C.-K.; Yuen, M.-F.; Zhang, T.-R.; Lee, C.-S.; Zhang, W.-J. Nickel−Cobalt Diselenide 3D Mesoporous Nanosheet Networks Supported on Ni Foam: An All-PH Highly Efficient Integrated Electrocatalyst for Hydrogen Evolution. *Adv. Mater.* **2017**, *29*, 1606521.

(60) Zhang, J.-J.; Zhao, T.-J.; Wang, H.-H.; Lin, Y.-X.; Zhai, G.-Y.; Jiang, Z.-D.; Hirano, S.-I.; Li, X.-H.; Chen, J.-S. Oriented Arrays of Co_3O_4 Nanoneedles for Highly Efficient Electrocatalytic Water Oxidation. *Chem. Commun.* **2019**, *55*, 3971−3974.

(61) Li, X.; Liu, P. F.; Zhang, L.; Zu, M. Y.; Yang, Y. X.; Yang, H. G. Enhancing Alkaline Hydrogen Evolution Reaction Activity through Ni−Mn_3O_4 Nanocomposites. *Chem. Commun.* **2016**, *52*, 10566−10569.

(62) Guan, D.; Ryu, G.; Hu, Z.; Zhou, J.; Dong, C.-L.; Huang, Y.-C.; Zhang, K.; Zhong, Y.; Komarek, A. C.; Zhu, M.; Wu, X.; Pao, C.-W.; Chang, C.-K.; Lin, H.-J.; Chen, C.-T.; Zhou, W.; Shao, Z. Utilizing Ion Leaching Effects for Achieving High Oxygen-Evolving Performance on Hybrid Nanocomposite with Self-Optimized Behaviors. *Nat. Commun.* **2020**, *11*, 3376.

(63) Hausmann, J. N.; Menezes, P. W. Effect of Surface-Adsorbed and Intercalated (Oxy) Anions on the Oxygen Evolution Reaction. *Angew. Chem., Int. Ed.* **2022**, *61*, No. e202207279.

(64) Dunitz, J. D.; Orgel, L. E. Electronic Properties of Transition-Metal Oxides-II: Cation Distribution amongst Octahedral and Tetrahedral Sites. *J. Phys. Chem. Solids* **1957**, *3*, 318−323.

(65) Speck, F. D.; Zagalskaya, A.; Alexandrov, V.; Cherevko, S. Periodicity in the Electrochemical Dissolution of Transition Metals. *Angew. Chem., Int. Ed.* **2021**, *60*, 13343−13349.

(66) Zhang, Z.; Li, W.; Ng, T.-W.; Kang, W.; Lee, C.-S.; Zhang, W. Iron(Ii) Molybdate ($FeMoO_4$) Nanorods as a High-Performance Anode for Lithium Ion Batteries: Structural and Chemical Evolution upon Cycling. *J. Mater. Chem. A* **2015**, *3*, 20527−20534.

(67) Bellato, F.; Ferri, M.; Annamalai, A.; Prato, M.; Leoncino, L.; Brescia, R.; De Trizio, L.; Manna, L. Colloidal Synthesis of Nickel Arsenide Nanocrystals for Electrochemical Water Splitting. *ACS Appl. Energy Mater.* **2023**, *6*, 151−159.

(68) Yu, Y.; Cheng, Y.; Guo, M.; Li, C.; Hu, J. Ag Nanoparticles Supported on Nickel Foam: A Flexible 3D Electrode for Methanol Electrocatalytic Oxidation. *RSC Adv.* **2017**, *7*, 39539−39545.

(69) Kang, Q.; Vernisse, L.; Remsing, R. C.; Thenuwara, A. C.; Shumlas, S. L.; McKendry, I. G.; Klein, M. L.; Borguet, E.; Zdilla, M. J.; Strongin, D. R. Effect of Interlayer Spacing on the Activity of Layered Manganese Oxide Bilayer Catalysts for the Oxygen Evolution Reaction. *J. Am. Chem. Soc.* **2017**, *139*, 1863−1870.

(70) McCrory, C. C. L.; Jung, S.; Peters, J. C.; Jaramillo, T. F. Benchmarking Heterogeneous Electrocatalysts for the Oxygen Evolution Reaction. *J. Am. Chem. Soc.* **2013**, *135*, 16977−16987.

(71) Doyle, R. L.; Lyons, M. E. G. An Electrochemical Impedance Study of the Oxygen Evolution Reaction at Hydrous Iron Oxide in Base. *Phys. Chem. Chem. Phys.* **2013**, *15*, 5224−5237.